Check for updates

APPLIED PHYSICS

Ultrafast decoherence in solid-state high-harmonic generation induced by nuclear-electronic entanglement

Shiqi Hu[1], Qing Chen[1,2], Ruiji Zhao[1], Qiuhao Xu[1], Qunfang Gu[1,2], En Wang[1,2], Sheng Meng[1,2,3]*

Copyright © 2026 The Authors, some rights reserved; exclusive licensee American Association for the Advancement of Science. No claim to original U.S. Government Works. Distributed under a Creative Commons Attribution NonCommercial License 4.0 (CC BY-NC).

High-harmonic generation (HHG) has provided groundbreaking insights into nonequilibrium dynamics involving strong light-matter interactions. However, intrinsic quantum effects of condensed matter, such as electronic coherence and its interplay with nuclear degrees of freedom—one of the most fascinating aspects of quantum mechanics—have largely been overlooked. Here, we explore the nuclear quantum effects (NQEs) on electronic coherence in solid-state HHG. Unlike classical nuclei, the strong delocalization of the nuclei caused by zero-point vibrations induces electronic decoherence on an ultrafast (attosecond to femtosecond) timescale through nuclear-electronic entanglement. In this manner, NQEs not only contribute to the ultrafast dephasing of HHG but also suppress the interband electron trajectory and thus switch the dominant mechanism from interband to intraband HHG in solids. This yields measurable signatures in HHG spectroscopy, enabling direct probe of coherence time and nuclear wave packets information in materials.

INTRODUCTION

The rise of attosecond science enables us to explore and understand quantum phenomena involving strong light-matter interactions. This encompasses one of the most fundamental problems in quantum mechanics: electronic coherence and its interplay with nuclear degrees of freedom (*1*–*7*). Although lighter electrons move faster on an attosecond timescale, nuclear states affect electron dynamics and quantum coherence through the topology of potential energy surfaces.

Recent photoionization studies (*8*–*13*) have revealed a close relationship between electronic coherence/decoherence in ionized molecular systems and electron-nucleus interactions. These interactions, encompassing both classical nuclear dynamics and quantum entanglement, subsequently govern charge migration and reaction pathways (*14*–*17*). Understanding the role of nuclear-electronic entanglement (NEE) in electronic decoherence, which remains an open question, is crucial for accessing, manipulating, and potentially performing Bell tests of quantum states (*18*–*21*). This is also pivotal in the ongoing quantum technology revolution in the fields such as quantum computing, quantum sensors, photochemistry, and optoelectronics (*2*, *22*–*24*).

As a prominent area of ultrafast and strong-field science, high-harmonic generation (HHG) occurs on an attosecond timescale before electronic coherence is lost (*25*, *26*). This makes HHG a potential avenue for investigating the interplay between electronic coherence and nuclear dynamics. In molecules and gases, the nuclear autocorrelation has been shown to modulate the electron recombination channels (*27*–*29*), thereby shaping the yield of different harmonics and extreme ultraviolet emissions (*30*).

Nevertheless, because of the multitude collective excitations and the complex interactions among them, the NEE has been largely ignored in solid materials despite that the community starts to realize the correlation between solid-state HHG and classical nuclear dynamics (*31*–*35*). This research gap has hindered a comprehensive understanding of solid-state HHG mechanisms, particularly regarding ultrafast dephasing and its impact on the competition between intraband and interband harmonic generation (*36*–*43*). In the first case, theoretical HHG spectra agree with experiments only when assuming an extremely fast dephasing time (few femtoseconds) (*36*–*43*), whereas experimental measurements of carrier lifetime and scattering rates (*44*–*49*) suggest that typical timescales are an order of magnitude longer than those assumed theoretically.

Although various mechanisms have been proposed to resolve this discrepancy—including macroscopic propagation effects (*50*), spatiotemporal filtering (*51*), real-space suppressing of long trajectories (*52*) and large electron-hole separations (*53*, *54*), electron momentum-dependent electron-phonon scattering (EPS) (*33*, *55*) and dephasing (*56*), and the influence of classical nuclear dynamics (*57*, *58*)—the origin of the ultrafast dephasing in HHG remains an open question.

In this work, we explore the quantum phenomena in attosecond processes via solid-state HHG, with a particular focus on NQEs and their role in driving quantum electronic systems toward statistical ensembles. This process occurs through ultrafast electronic decoherence (~1 fs) within the framework of NEE (*59*–*67*). The decoherence induced by NQEs represents a potential physical origin for the ultrafast dephasing observed in solid-state HHG, leading to distinct changes in the relative contributions of intraband and interband harmonics that are different from those in gas-phase systems. Investigations into these dynamics enable not only potential insights in understanding recent HHG experiments (*68*, *69*) but also the direct probing of quantum coherence time and nuclear wave packets (NWPs) in solid materials.

RESULTS AND DISCUSSION

The NQE-induced decoherence of HHG has been first investigated in the high-pressure superconductor Im-3m H3S (Fig. 1A). Im-3m H3S serves as a prototype example where the strong NQEs of hydrogen (H) atoms enhance lattice stabilization and superconductivity. The NQEs, notably the zero-point motions, strongly affect the nuclear delocalization $<\Delta R^2>^{1/2} = <\Delta R_x^2 + \Delta R_y^2 + \Delta R_z^2>^{1/2}$. Here $\Delta R_{x,y,z}$ is the nuclei displacement along different directions, which is described by the Gaussian distribution centered around equilibrium position (fig. S9). Figure 1 (A and B) gives the probability distributions

[1]Beijing National Laboratory for Condensed Matter Physics and Institute of Physics, Chinese Academy of Sciences, Beijing 100190, P. R. China. [2]School of Physical Sciences, University of Chinese Academy of Sciences, Beijing 100049, P. R. China. [3]Songshan Lake Materials Laboratory, Dongguan, Guangdong 523808, P. R. China. *Corresponding author. Email: smeng@iphy.ac.cn

Downloaded from https://www.science.org at Institute of Physics, Cas on November 07, 2026

of $<\Delta R^2>^{1/2}$ for sulfur (S) and H nuclei, where the peaks show the most probable nuclear delocalization $<\Delta R^2>^{1/2}_{max}$ and $\sigma_{\Delta R}$ denotes the delocalization width. For S nuclei, $<\Delta R^2>^{1/2}_{max}$ increases slightly from 0.08 Å without NQEs to 0.10 Å with NQEs included. In contrast, the light H nuclei—whose vibration frequency can surpass its thermal energy by an order of magnitude—gives a large superposition of NWPs, resulting in a notable enhancement in nuclear delocalization. Therefore, the $<\Delta R^2>^{1/2}_{max}$ of H nuclei shifts from 0.12 to 0.22 Å, and $\sigma_{\Delta R}$ shifts from 0.08 to 0.19 Å when NQEs are considered.

On the other hand, the large quantum fluctuations induce the electron rearrangement around the H nuclei, which alters the screening and thus modulates the potential energy surface of the H—S bond (figs. S7 and S8). This ultimately amplifies structural disorder and phonon anharmonicity. As shown in Fig. 1C, the spectrum of velocity autocorrelation function C_{vv} of atom oscillations, which denotes the phonon density of states, shows the emergence of anharmonic phonon peak involving H nuclei (*70*–*73*) at ~0.24 eV, aligning well with recent studies (*71*–*73*). As a result, the charge density oscillations exhibit faster decay as shown in Fig. 1 (D and E).

In Fig. 2A, the HHG spectra along the [100] direction of H_3S are depicted both with and without NQEs. For comparison, we plot the HHG spectra without NQEs but with a phenomenological decoherence. This is achieved by artificially setting the decoherence time T_2 to ~1 fs in simulations, where T_2 quantifies the decay time of the off-diagonal elements of the electron density matrix. For subsequent discussions and figures on HHG with/without NQEs, T_2 is set to infinity by default unless stated explicitly, indicating that no intrinsic electronic decoherence is considered. In the absence of NQEs or finite T_2, the harmonics exhibit a noisy spectral configuration, with small splits appearing in the HHG peaks. In contrast, the inclusion of NQEs or a phenomenological T_2 gives visible harmonic peaks.

As shown in Fig. 2 (B and C), similar to recent experiments (*74*–*76*), for low-order HHG, such as the fifth harmonic, the intensity increases with the electron doping level n in all the cases. However, for the high-order interband HHG (e.g., the 11th harmonic), whose intensity decreases with n, the inclusion of NQEs completely reverses the doping dependence.

As illustrated in Fig. 2 (D and E), for intraband fifth harmonics whose intensity is proportional to the carrier concentration n, NQEs do not alter the generation mechanism, thereby maintaining the doping dependence. In contrast, for interband 11th harmonics, whose intensity decreases with n due to the hindered recombination caused by either Pauli-blocking effects (*74*) or dephasing from incoherent doped-carriers (*75*, *76*), NQEs effectively switch the mechanism from interband to intraband dynamics by largely suppressing the interband contributions. Consequently, the doping dependence is reversed.

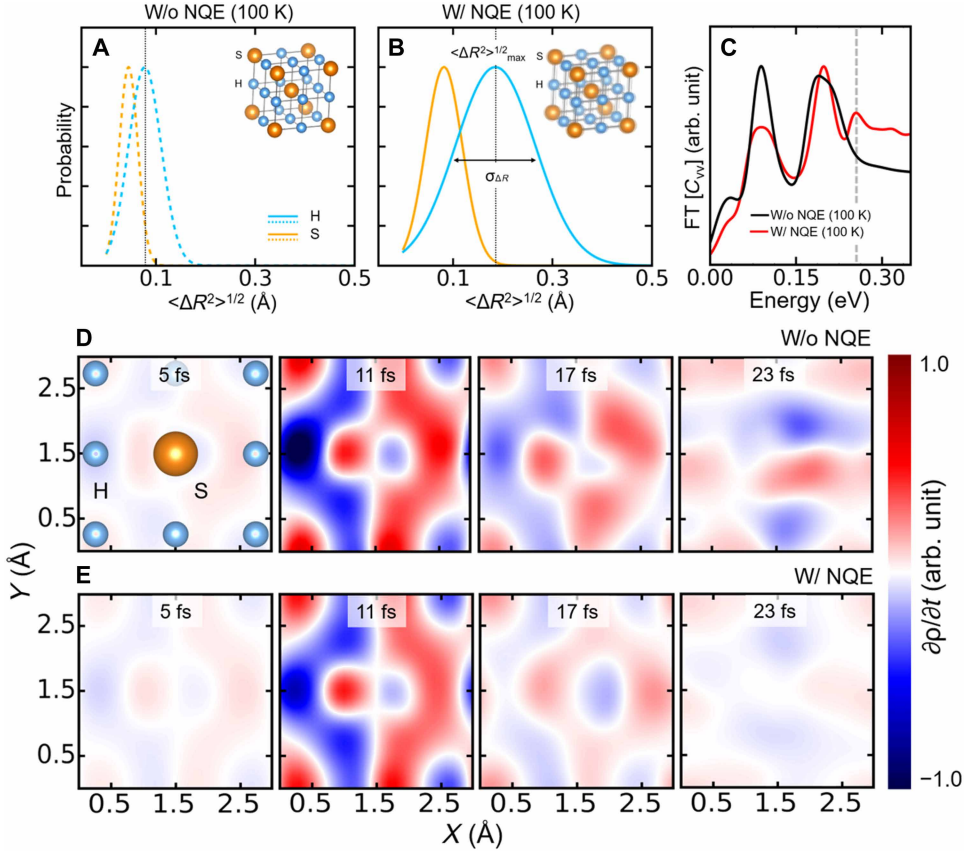


Fig. 1. The NQEs in Im-3m H_3S. Probability distributions of nuclear delocalization $<\Delta R^2>^{1/2}$ without NQEs (**A**) and with NQEs (**B**) at 100 K. The distribution peaks (labeled by black dotted lines) is the most probable nuclear delocalization $<\Delta R^2>^{1/2}_{max}$, and $\sigma_{\Delta R}$ is the delocalization width. The inset schematics show the lattice structure of Im-3m H_3S without and with NQEs. (**C**) Spectrum of velocity autocorrelation function of atom displacement oscillations C_{vv}. The gray dashed line labels the anharmonic phonon peak involving H nuclei. The carrier density dynamics induced by laser at (001) plane without (**D**) and with (**E**) NQEs. The central time of the laser envelope $t_0 = 12$ fs. The without NQEs (w/o NQE) case is based on thermal ensembles, which only include the thermal fluctuations of classical nuclear motions.

Downloaded from https://www.science.org at Institute of Physics, Cas on November 07, 2026

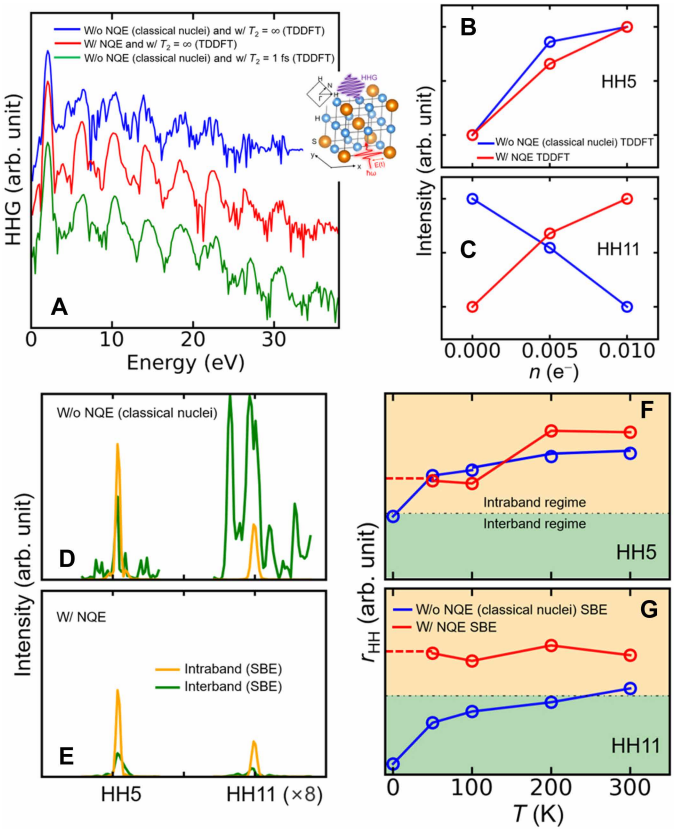


Fig. 2. HHG dynamics in Im-3m H_3S. (**A**) HHG spectra of Im-3m H_3S with and without NQEs. The inset denotes a schematic of HHG process. The normalized intensity of 5th (**B**) and 11th (**C**) harmonic as a function of electron doping with and without NQEs. The interband and intraband contributions of 5th and 11th harmonic, without (**D**) and with NQEs (**E**). The phase diagram on dominant yielding mechanism of 5th (**F**) and 11th (**G**) harmonic with and without NQEs. The dashed line is an extension line. The without NQEs (w/o NQE) case is based on thermal ensembles, which only include the thermal fluctuations of classical nuclear motions. The HHG in (A) to (C) is obtained from the time-dependent density functional theory (TDDFT) calculations, while the analysis in (D) and (F) is obtained by semiclassical Bloch equation (SBE).

By defining $r_{HH} = I_{intraband}/I_{interband}$, where $I_{intraband}$ ($I_{interband}$) is the intensity of intraband (interband) component of HHG, we obtain the phase diagram of HHG mechanism in Fig. 2 (F and G). Here, $r_{HH} > 1$ ($r_{HH} < 1$) denotes the intraband (interband) dominant regime of harmonic generation, respectively. The NQE-induced intra- and interband HHG transitions appears to be quite robust across various temperatures. While at high temperatures thermal effects result in a smaller regime for transitions, their impact remains quite limited (fig. S5). These results indicate that, unlike the three-step model of gas-phase HHG (*77*), NQEs play a decisive role in determining the intraband and interband mechanisms of solid-state HHG.

In solids, the multiple recombination of excited electron-hole pairs generates long and short trajectories of interband HHG emission. As depicted in time-frequency spectrogram in Fig. 3 (A and B), the persistent electronic coherences result in strong quantum interference between the interband trajectories, introducing chirps in post-pulse HHG emission and thus peak splitting in spectrum (*36*–*40*). By contrast, the inclusion of NQEs reduces the high-energy (above ninth harmonics, >18 eV) and postpulse HHG emission (Fig. 3B), making the HHG spectrum "clean" (Fig. 2A).

The result suggests a significant suppression of electronic coherence and, consequently, the interband trajectories (*36*–*40*). To illustrate this, we compare the time-frequency trajectories of harmonics associated with NQEs to those without NQEs but with an artificially set decoherence time ($T_2 \sim 1$ fs) in Fig. 3D. The trajectories show good agreement with each other (also see the similar spectra in Fig. 2A and fig. S6). This scenario is further confirmed by examining the population evolution of the photoexcited electron in Fig. 3C. Different from the phonon-enhanced photocarrier doping mechanism (*78*) in classical nuclei case, the greater population accumulation in the presence of NQEs originates from suppressed electron-hole recombination, a consequence of the NQE-enhanced electronic decoherence (*79*).

Recent studies show that propagation effects (*50*) and EPS (*33*) also contribute to HHG dephasing. However, the propagation effect requires a large propagation length of ~10 μm (*50*), while many HHG spectra are done in atomically thin samples. The dephasing time from EPS is usually several to tens of femtoseconds (*33*), much longer than our case. At low temperatures, the EPS-induced dephasing is even weaker, while NQEs are more significant. Therefore, NQEs are expected to be a dominant source of electronic decoherence in HHG.

The NQE-induced electronic decoherence can be understood by the NEE effect, where the electron coherence is taken away by the quantum evolution of nucleus subsystem (*6*, *59*–*61*). The total wave function of entangled electron-nucleus system is written as: $|\Psi(\mathbf{r},\mathbf{R},t)\rangle = \sum_i |\phi_i(\mathbf{r},\mathbf{R})\rangle|\chi_i(\mathbf{R},t)\rangle$, where $|\phi_i(\mathbf{r},\mathbf{R})\rangle$ is the ith eigenstate of the electronic Hamiltonian $\hat{H}^e(\mathbf{R})$, while $|\chi_i(\mathbf{R},t)\rangle$ is the NWP associated with the electronic state. The electronic coherence is contained in the off-diagonal elements of the electron density matrix: $\hat{\rho}^e_{ii'}(t) = |\phi_i(\mathbf{r},\mathbf{R})\rangle\langle\phi_{i'}(\mathbf{r},\mathbf{R})|\langle\chi_{i'}(\mathbf{R},t)|\chi_i(\mathbf{R},t)\rangle = |\phi_i(\mathbf{r},\mathbf{R})\rangle\langle\phi_{i'}(\mathbf{r},\mathbf{R})|\langle\chi(0)|\exp\{i\left[\hat{H}^e_i(\mathbf{R}) - \hat{H}^e_{i'}(\mathbf{R})\right]t/\hbar\}|\chi(0)\rangle$, where $\exp\left\{i\left[\hat{H}^e_i(\mathbf{R}) - \hat{H}^e_{i'}(\mathbf{R})\right]t/\hbar\right\}|\chi(0)\rangle$ describes the NWP propagation on the ith electronic surface (*59*–*63*). The electronic coherence is lost whenever $\hat{\rho}^e_{ii'} = 0$, which can be achieved either from density matrix of electron part, i.e., $|\phi_i(\mathbf{r},\mathbf{R})\rangle\langle\phi_{i'}(\mathbf{r},\mathbf{R})|$, or from the NWP when $\langle\chi(0)|\exp\left\{i\left[\hat{H}^e_i(\mathbf{R}) - \hat{H}^e_{i'}(\mathbf{R})\right]t/\hbar\right\}|\chi(0)\rangle$ vanishes, as discussed here.

We quantify this NQE-induced decoherence by calculating the purity of electron density matrix ρ^e in the presence of NWP obtained by quantum mechanical dynamics (QMD). The purity is defined as $P = \mathrm{Tr}\left(\left[\rho^e\right]^2\right)$. $P = 1$ represents the pure quantum state, while $P = 0$ means complete decoherence. As shown in Fig. 3C, after laser excitation, the dynamics of NWP leads to an attosecond electronic decoherence within 1 fs. The NWP collapses during the evolution, resulting in phase mismatch of different components and the nucleus delocalization (Fig. 3, E and F). The electronic decoherence naturally originates from (i) the dephasing and (ii) the decay in overlap of different components of delocalized NWP (*62*–*67*). This NQE-induced decoherence is also manifested the electron dynamics in real space (Fig. 1, D and E), and with NQEs, the charge density oscillations induced by laser exhibit faster decay.

This scenario is also reflected in the time-frequency spectrum of HHG, as shown in Fig. 3D. For the fifth harmonics, the phase

Downloaded from https://www.science.org at Institute of Physics, Cas on November 07, 2026

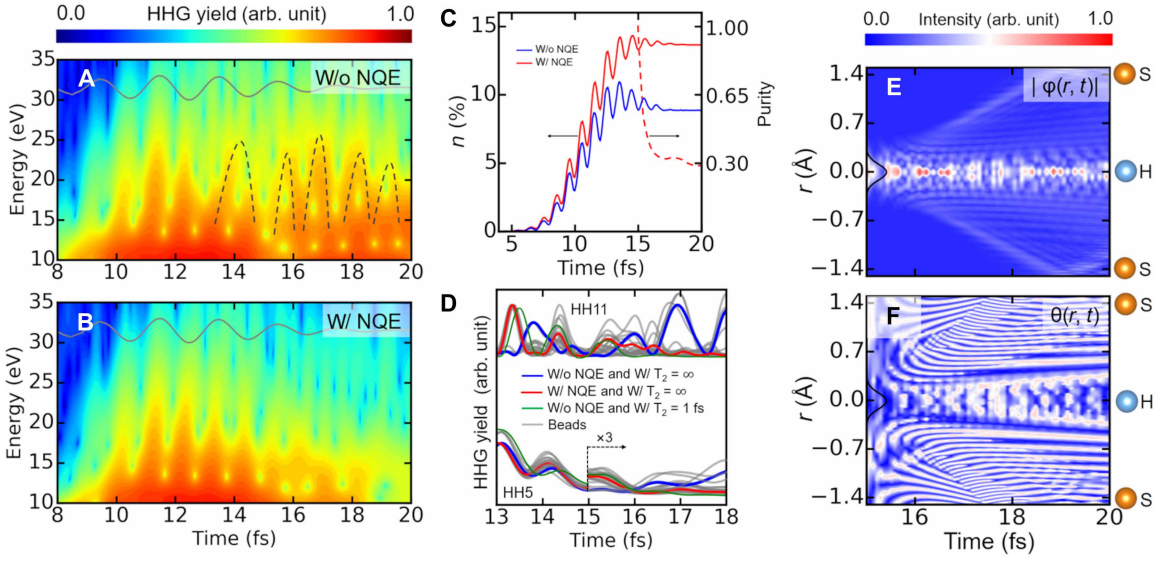


Fig. 3. The NEE and its effects on HHG. The time-frequency spectrograms of HHG in H_3S without (**A**) and with (**B**) NQEs obtained from TDDFT. The gray solid curves label the oscillation of laser field. The black dashed lines, which serve as a guide to the eye, mark the short and long trajectories of HHG emission. (**C**) Electronic population obtained from TDDFT and coherence (purity) obtained from QMD as a function of time with laser excitation. (**D**) Time-frequency analysis of 5th and 11th HHG with and without NQEs obtained from TDDFT. The gray lines denote the results for various beads, whereas the green line indicates the results without NQEs but with the presence of the phenomenological decoherence time $T_2 \sim 1$ fs. The evolution of profile (**E**) and phase (**F**) of the NWP obtained from QMD. The black lines mark the distribution of initial NWP. The without NQEs (w/o NQE) case is based on thermal ensembles, which only include the thermal fluctuations of classical nuclear motions.

cancellation of NWP has no effect, as the intraband HHG relies on carrier population (i.e., the diagonal elements of ρ^e). The HHG trajectories from different beads exhibit in-phase behaviors. In contrast, for the 11th interband harmonics, which depend on the transition dipole moment (i.e., the off-diagonal elements of ρ^e), the HHG trajectories of beads have different phases and cancel each other out, especially in the tail of the laser pulse (after 15 fs). This leads to electronic decoherence and suppression of interband harmonics.

By suppressing the interference between HHG trajectories, NQEs give a one-to-one mapping between harmonic frequency and generation time (at least in each subcycle), with longer times producing higher frequencies (Fig. 4A) (*26*–*28*). Because the intensity of interband harmonics changes identically with electronic coherence (purity), as shown in Fig. 4B, by fitting the time-dependent harmonic intensities $|I_{HH}|^2$, the time of NQE-induced decoherence, T_2^{NQE}, can be directly probed. The retrieved T_2^{NQE} is ~1.0 fs, consistent with the decoherence time fitting from purity evolution, which is around 0.9 fs.

The decoherence dynamics were further investigated from the HHG under different temperatures/hydrogen isotopes in Fig. 4 (C and D). The retrieved T_2^{NQE} show good agreement with those obtained from purity evolution via QMD. The effect of temperature/isotope in QMD is introduced by changing the size of the initial NWP. Compared to the classical case, NQEs significantly accelerate electron decoherence by an order of magnitude. As the temperature decreases, nuclear delocalization due to thermal effects diminishes, zero-point vibrations that are temperature-independent become dominant, and the decoherence time tends to converge to a constant. A similar dependence is observed for different isotopes.

Moreover, the decoherence time T_2^{NQE} induced by NQEs shows identical temperature and isotope dependence with the inverse of the nucleus delocalization width $\sigma_{\Delta R}{}^{-1}$, i.e., $T_2^{NQE} \propto \sigma_{\Delta R}{}^{-1}$ (Fig. 1B). Since the delocalization $\sigma_{\Delta R}$ indicates the effective width of NWP, this relationship justifies the frozen Gaussian framework (*62*, *63*, *80*), which in turn enables the direct measurement of NWP width using HHG spectroscopy.

Given the universality of zero-point vibrations, we extended our study to various materials. The NQEs are found to significantly modify HHG spectra and decoherence dynamics (figs. S10 and S11), demonstrating their broad applicability. A general linear relationship between $\sigma_{\Delta R}$, T_2, and $\sqrt{(M_v\omega)}$ is revealed among different materials, where M_v is the averaged atomic mass and ω is the nuclear vibration frequency. The relationship can be understood by the characteristic length of the quantum harmonic oscillator wave function: $\frac{1}{2}M_v\omega^2\Delta R^2 \propto \left(\frac{1}{2}+n\right)\hbar\omega$, where n satisfies the Bose-Einstein distribution at a specific temperature and ΔR is the nuclear amplitude that is approximately proportional to delocalization width $\sigma_{\Delta R}$. Therefore, $\Delta R^{-1} \propto \sigma_{\Delta R}^{-1} \propto \sqrt{M_v\omega}$, which allows us to estimate decoherence time through the static properties of the system, as shown in fig. S11.

Last, we discuss the experimental observations of NQEs in HHG. Although more HHG experiments are needed in the future for various materials including H_3S, it is a good alternative to reexamine the readily available HHG experiments of light-element solids with large NQE, e.g., graphene (*81*, *82*). In figs. S10 and S11 and S18, we investigate the NQE and its effects on HHG in graphene. Thanks to high zero-point energy of carbon atoms (~0.1 eV), NQEs contribute to the delocalization of carbon nuclei even at room temperature. NQEs affect the spectroscopic distribution and elliptical polarization angle of various harmonics, producing the HHG spectra that are in good agreement with recent experiments (*68*, *69*). These results suggest that NQEs may constitute an important contribution to the anomalous

Downloaded from https://www.science.org at Institute of Physics, Cas on November 07, 2026

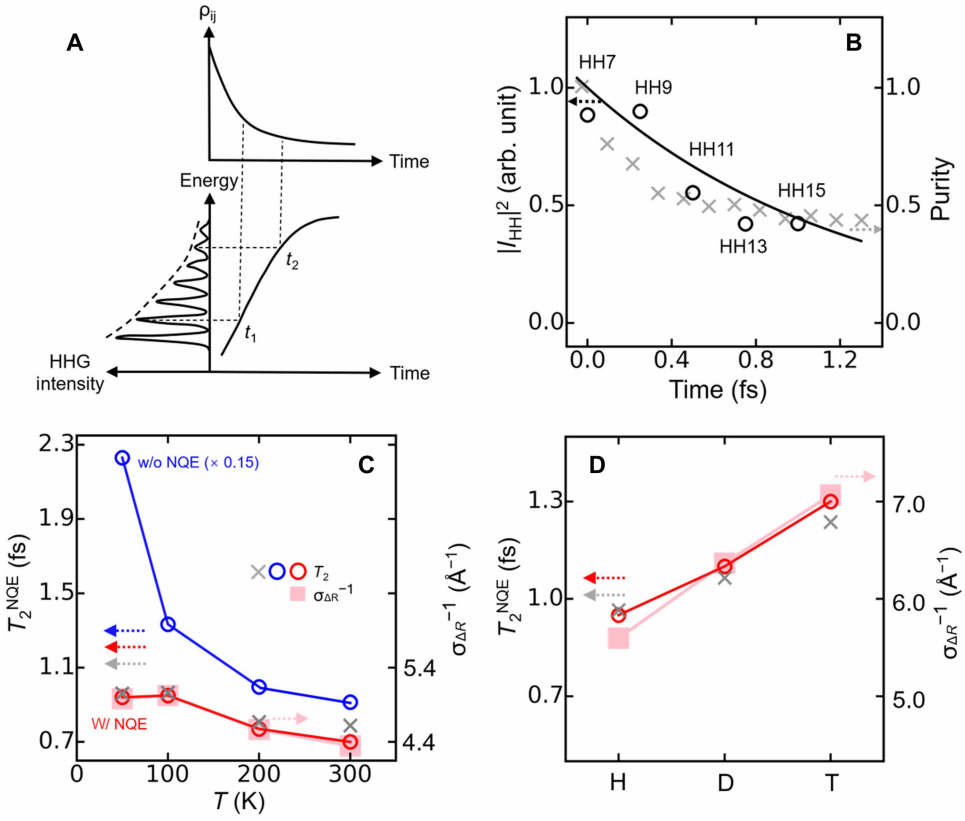


Fig. 4. Retrieve decoherence time from HHG spectroscopy. (**A**) Schematics showing encoding of electronic coherence within time-frequency spectrograms of HHG. The decoherence over time corresponds to higher harmonics yield. (**B**) Normalized intensity of different harmonics $|I_{HH}|^2$ and electronic coherence (purity) as a function of time in H_3S. The black line is the fitting using exp.[$-t/T_2^{NQE}$]. The retrieved T_2^{NQE} and $\sigma_{\Delta R}^{-1}$ as a function of temperature (**C**) and H isotope masses (**D**) obtained from TDDFT. The gray crosses label the T_2^{NQE} obtained from QMD. The without NQEs (w/o NQE) case is based on thermal ensembles, which only include the thermal fluctuations of classical nuclear motions.

ellipticity dependence observed in experimental graphene HHG (*68, 69*).

MATERIALS AND METHODS

The NQE-induced decoherence of HHG has been first investigated in the high-pressure superconductor Im-3m H_3S (Fig. 1A) (*70–72, 83, 84*). Im-3m H_3S serves as a prototype example where the strong NQEs of H atoms enhance lattice stabilization and superconductivity (*70–72*). Ring-polymer molecular dynamics (RPMD) (*85, 86*) and ab initio molecular dynamics (AIMD) are used at different temperatures (50 to 300 K) to account for NQEs and classical thermal effects, respectively. These effects are taken into consideration by sampling the distorted lattice generated from a variety of molecular dynamics trajectories (*57*).

To study HHG, we combine AIMD and RPMD with first-principles time-dependent density functional theory simulations and semiclassical Bloch equation calculations (*87, 88*). For Im-3m H_3S system, a linearly polarized laser pulse with Gaussian envelope electric field $\mathbf{F}(t) = \mathbf{F}_0\cos(\omega t)\exp\left[-\left(t-t_0\right)^2/2\sigma^2\right]$ is adopted with ω ~2.0 eV, σ ~6.0 fs, $t_0 = 12$ fs, and $\mathbf{F}_0$ ~ 0.9 V/Å. For graphene, an elliptical polarized laser pulse with Gaussian envelope electric field $\mathbf{F}(t) = \mathbf{F}_0\left(1+\varepsilon^2\right)^{-1/2}\exp\left[-\left(t-t_0\right)^2/2\sigma^2\right](\cos\omega t, \varepsilon\sin\omega t)$ is adopted in graphene plane with ω ~0.26 eV, σ ~28.0 fs, $t_0 = 100$ fs, $\varepsilon = 0.3$, and $\mathbf{F}_0$ ~ 0.2 V/Å. By adding the vector potential $\mathbf{A}(t) = -c\int \mathbf{F}(t')dt'$ in the Hamiltonian and evolving the electronic wave functions in real time, the HHG spectra are obtained through the Fourier transform of time-dependent current $\mathbf{j}(t) = -\frac{e}{m}\int d\mathbf{r}\,\{\psi^*(\mathbf{r},t)[-i\hbar\nabla + e\mathbf{A}(t)]\psi(\mathbf{r},t) + c.c.\}$. To track the NQE-induced electronic decoherence and NEE in H_3S, the time-dependent Schrödinger equation of nucleus-electron–coupled system is solved on the basis of the Born-Huang expansion, and we call it a QMD model (*89*). See Supplementary Materials for more details.

Supplementary Materials

This PDF file includes:

Notes S1 to S4
Figs. S1 to S18
References

REFERENCES

1. A. Ekert, P. L. Knight, Entangled quantum systems and the Schmidt decomposition. *Am. J. Phys.* **63**, 415–423 (1995).
2. A. M. Nielsen, I. L. Chuang, *Quantum Computation and Quantum Information* (Cambridge Univ. Press, 2010).

Downloaded from https://www.science.org at Institute of Physics, Cas on November 07, 2026

3. R. Horodecki, P. Horodecki, M. Horodecki, K. Horodecki, Quantum entanglement. *Rev. Mod. Phys.* **81**, 865–942 (2009).
4. C. Zhu, S. Nangia, A. W. Jasper, D. G. Truhlar, Coherent switching with decay of mixing: An improved treatment of electronic coherence for non-Born–Oppenheimer trajectories. *J. Chem. Phys.* **121**, 7658–7670 (2004).
5. M. Vacher, D. Mendive-Tapia, M. J. Bearpark, M. A. Robb, The second-order Ehrenfest method. *Theor. Chem. Acc.* **133**, 1505 (2014).
6. L. Cruz-Rodriguez, D. Dey, A. Freibert, P. Stammer, Quantum phenomena in attosecond science. *Nat. Rev. Phys.* **6**, 691–704 (2024).
7. S. K. Min, F. Agostini, E. K. U. Gross, Coupled-trajectory quantum-classical approach to electronic decoherence in nonadiabatic processes. *Phys. Rev. Lett.* **115**, 073001 (2015).
8. L.-M. Koll, L. Maikowski, L. Drescher, T. Witting, M. J. J. Vrakking, Experimental control of quantum-mechanical entanglement in an attosecond pump-probe experiment. *Phys. Rev. Lett.* **128**, 043201 (2022).
9. T. Nishi, E. Lötstedt, K. Yamanouchi, Entanglement and coherence in photoionization of H_2 by an ultrashort XUV laser pulse. *Phys. Rev. A* **100**, 013421 (2019).
10. Y. Nabekawa, K. Midorikawa, Analysis of attosecond entanglement and coherence using feasible formulae. *Phys. Rev. Res.* **5**, 033083 (2023).
11. A. S. Maxwell, L. B. Madsen, M. Lewenstein, Entanglement of orbital angular momentum in non-sequential double ionization. *Nat. Commun.* **13**, 4706 (2022).
12. E. Goulielmakis, Z.-H. Loh, A. Wirth, R. Santra, N. Rohringer, V. S. Yakovlev, S. Zherebtsov, T. Pfeifer, A. M. Azzeer, M. F. Kling, S. R. Leone, F. Krausz, Real-time observation of valence electron motion. *Nature* **466**, 739–743 (2010).
13. D. Younis, S. Xie, J. H. Eberly, Quantum entanglement during single-cycle nonsequential ionization. arXiv:2403.09854 [physics.atom-ph]; https://doi.org/10.48550/arXiv.2403.09854.
14. J. Breidbach, L. S. Cederbaum, Migration of holes: Formalism, mechanisms, and illustrative applications. *J. Chem. Phys.* **118**, 3983–3996 (2003).
15. I. K. Alexander, S. Lünnemann, S. Lorenz, Ultrafast charge migration following valence ionization of 4-methylphenol: Jumping over the aromatic ring. *J. Phys. Chem. A* **114**, 8676–8679 (2010).
16. R. D. Martin Blavier, Time evolution of entanglement of electrons and nuclei and partial traces in ultrafast photochemistry. *Phys. Chem. Chem. Phys.* **24**, 17516–17525 (2022).
17. D. T. Matselyukh, V. Despré, N. V. Golubev, A. I. Kuleff, H. J. Wörner, Decoherence and revival in attosecond charge migration driven by non-adiabatic dynamics. *Nat. Phys.* **18**, 1206–1213 (2022).
18. M. J. J. Vrakking, Control of attosecond entanglement and coherence. *Phys. Rev. Lett.* **126**, 113203 (2021).
19. D. Dey, A. I. Kuleff, G. A. Worth, Quantum interference paves the way for long-lived electronic coherences. *Phys. Rev. Lett.* **129**, 173203 (2022).
20. C. Bourassin-Bouchet, L. Barreau, V. Gruson, J.-F. Hergott, F. Quéré, P. Salières, T. Ruchon, Quantifying decoherence in attosecond metrology. *Phys. Rev. X* **10**, 031048 (2020).
21. M. Ruberti, V. Averbukh, F. Mintert, Bell test of quantum entanglement in attosecond photoionization. *Phys. Rev. X* **14**, 041042 (2024).
22. P. W. Shor, Algorithms for quantum computation: discrete logarithms and factoring, in *Proceedings 35th Annual Symposium on Foundations of Computer Science* (IEEE, 1994), pp. 124–134.
23. A. K. Ekert, Quantum cryptography based on Bell's theorem. *Phys. Rev. Lett.* **67**, 661–663 (1991).
24. D. Bouwmeester, J.-W. Pan, K. Mattle, M. Eibl, H. Weinfurter, A. Zeilinger, Experimental quantum teleportation. *Nature* **390**, 575–579 (1997).
25. F. Krausz, M. Ivanov, Attosecond physics. *Rev. Mod. Phys.* **81**, 163–234 (2009).
26. S. Y. Kruchinin, F. Krausz, V. S. Yakovlev, Colloquium: Strong-field phenomena in periodic systems. *Rev. Mod. Phys.* **90**, 021002 (2018).
27. M. Lein, Attosecond probing of vibrational dynamics with high-harmonic generation. *Phys. Rev. Lett.* **94**, 053004 (2005).
28. S. Baker, J. S. Robinson, C. A. Haworth, H. Teng, R. A. Smith, C. C. Chirilă, M. Lein, J. W. G. Tisch, J. P. Marangos, Probing proton dynamics in molecules on an attosecond time scale. *Science* **312**, 424–427 (2006).
29. W. Li, X. Zhou, R. Lock, S. Patchkovskii, A. Stolow, H. C. Kapteyn, M. M. Murnane, Time-resolved dynamics in N_2O_4 probed using high harmonic generation. *Science* **322**, 1207–1211 (2008).
30. A. Ferré, H. Soifer, O. Pedatzur, C. Bourassin-Bouchet, B. D. Bruner, R. Canonge, F. Catoire, D. Descamps, B. Fabre, E. Mével, S. Petit, N. Dudovich, Y. Mairesse, Two-dimensional frequency resolved optomolecular gating of high-order harmonic generation. *Phys. Rev. Lett.* **116**, 053002 (2016).
31. H. Shi-Qi, H. Zhao, X.-B. Liu, Q. Chen, D.-Q. Chen, X.-Y. Zhang, S. Meng, Phonon-coupled high-harmonic generation for exploring nonadiabatic electron-phonon interactions. *Phys. Rev. Lett.* **133**, 156901 (2024).
32. J. Zhang, Z. Wang, F. Lengers, D. Wigger, D. E. Reiter, T. Kuhn, H. J. Wörner, T. T. Luu, High-harmonic spectroscopy probes lattice dynamics. *Nat. Photonics* **18**, 792–798 (2024).
33. V. Korolev, T. Lettau, V. Krishna, A. Croy, M. Zuerch, C. Spielmann, M. Waechtler, U. Peschel, S. Graefe, G. Soavi, D. Kartashov, Unveiling the role of electron-phonon scattering in dephasing high-order harmonics in solids. arXiv:2401.12929 [physics.optics]; https://arxiv.org/abs/2401.12929.
34. O. Neufeld, J. Zhang, U. De Giovannini, H. Hübener, A. Rubio, Probing phonon dynamics with multidimensional high harmonic carrier-envelope-phase spectroscopy. *Proc. Natl. Acad. Sci. U.S.A.* **119**, e2204219119 (2022).
35. M. R. Bionta, E. Haddad, A. Leblanc, V. Gruson, P. Lassonde, H. Ibrahim, J. Chaillou, N. Émond, M. R. Otto, Á. Jiménez-Galán, R. E. F. Silva, M. Ivanov, B. J. Siwick, M. Chaker, F. Légaré, Tracking ultrafast solid-state dynamics using high harmonic spectroscopy. *Phys. Rev. Res.* **3**, 023250 (2021).
36. G. Vampa, C. R. McDonald, G. Orlando, P. B. Corkum, T. Brabec, Semiclassical analysis of high harmonic generation in bulk crystals. *Phys. Rev. B* **91**, 064302 (2015).
37. G. Vampa, C. R. McDonald, G. Orlando, D. D. Klug, P. B. Corkum, T. Brabec, Theoretical analysis of high-harmonic generation in solids. *Phys. Rev. Lett.* **113**, 073901 (2014).
38. Y. W. Kim, T. Shao, H. Kim, S. Han, M. Seungchul Kim, X.-B. B. Ciappina, S.-W. Kim, Spectral interference in high harmonic generation from solids. *ACS Photonics* **6**, 851–857 (2019).
39. T.-Y. Du, Probing the dephasing time of crystals via spectral properties of high-order harmonic generation. *Phys. Rev. A* **100**, 053401 (2019).
40. W. Mengxi, S. Ghimire, D. A. Reis, K. J. Schafer, M. B. Gaarde, High-harmonic generation from Bloch electrons in solids. *Phys. Rev. A* **91**, 043839 (2015).
41. M. Hohenleutner, F. Langer, O. Schubert, M. Knorr, U. Huttner, S. W. Koch, M. Kira, R. Huber, Real-time observation of interfering crystal electrons in high-harmonic generation. *Nature* **523**, 572–575 (2015).
42. T. T. Luu, H. J. Wörner, High-order harmonic generation in solids: A unifying approach. *Phys. Rev. B* **94**, 115164 (2016).
43. Y. Chao, X. Zhang, X. Shicheng Jiang, G. Y. Cao, W. Tong, L. Bai, L. Ruifeng, Dependence of high-order-harmonic generation on dipole moment in SiO_2 crystals. *Phys. Rev. A* **94**, 013846 (2016).
44. J. L. Oudar, D. Hulin, A. Migus, A. Antonetti, F. Alexandre, Subpicosecond spectral hole burning due to nonthermalized photoexcited carriers in gaas. *Phys. Rev. Lett.* **55**, 2074–2077 (1985).
45. P. C. Becker, H. L. Fragnito, C. H. Brito Cruz, R. L. Fork, J. E. Cunningham, J. E. Henry, C. V. Shank, Femtosecond photon echoes from band-to-band transitions in GaAs. *Phys. Rev. Lett.* **61**, 1647–1649 (1988).
46. T. P. H. Sidiropoulos, N. Di Palo, D. E. Rivas, S. Severino, M. Reduzzi, B. Nandy, B. Bauerhenne, S. Krylow, T. Vasileiadis, T. Danz, P. Elliott, S. Sharma, K. Dewhurst, C. Ropers, Y. Joly, M. E. Garcia, M. Wolf, R. Ernstorfer, Probing the energy conversion pathways between light, carriers, and lattice in real time with attosecond core-level spectroscopy. *Phys. Rev. X* **11**, 041060 (2021).
47. G. Rohde, A. Stange, A. Muller, M. Behrendt, L.-P. Oloff, K. Hanff, T. J. Albert, P. Hein, K. Rossnagel, M. Bauer, Ultrafast formation of a fermi-dirac distributed electron gas. *Phys. Rev. Lett.* **121**, 256401 (2018).
48. A. Block, M. Liebel, R. Yu, M. Spector, Y. Sivan, F. J. García de Abajo, N. F. van Hulst, Tracking ultrafast hot-electron diffusion in space and time by ultrafast thermomodulation microscopy. *Sci. Adv.* **5**, eaav8965 (2019).
49. J. Sjakste, K. Tanimura, G. Barbarino, L. Perfetti, N. Vast, Hot electron relaxation dynamics in semiconductors: Assessing the strength of the electron–phonon coupling from the theoretical and experimental viewpoints. *J. Phys. Condens. Matter* **30**, 353001 (2018).
50. I. Kilen, M. Kolesik, J. Hader, J. V. Moloney, U. Huttner, M. K. Hagen, S. W. Koch, Propagation induced dephasing in semiconductor high-harmonic generation. *Phys. Rev. Lett.* **125**, 083901 (2020).
51. C. Q. Abadie, W. Mengxi, M. B. Gaarde, Spatiotemporal filtering of high harmonics in solids. *Opt. Lett.* **43**, 5339–5342 (2018).
52. G. G. Brown, Á. Jiménez-Galán, R. E. F. Silva, M. Ivanov, Ultrafast dephasing in solid-state high harmonic generation: Macroscopic origin revealed by real-space dynamics. *J. Opt. Soc. Am. B* **41**, B40–B46 (2024).
53. G. G. Brown, Á. Jiménez-Galán, R. E. F. Silva, M. Ivanov, Real-space perspective on dephasing in solid-state high harmonic generation. *Phys. Rev. Res.* **6**, 043005 (2024).
54. G. Wang, D. Tao-Yuan, Quantum decoherence in high-order harmonic generation from solids. *Phys. Rev. A* **103**, 063109 (2021).
55. K. Lively, S. A. Sato, G. Albareda, A. Rubio, A. Kelly, Revealing ultrafast phonon mediated inter-valley scattering through transient absorption and high harmonic spectroscopies. *Phys. Rev. Res.* **6**, 013069 (2024).
56. M. Kolesik, J. V. Moloney, Numerical discreteness and dephasing in high-harmonic calculations in solids. *Phys. Rev. B* **108**, 115433 (2023).
57. D. Freeman, A. Kheifets, S. Yamada, A. Yamada, K. Yabana, High-order harmonic generation in semiconductors driven at near- and mid-infrared wavelengths. *Phys. Rev. B* **106**, 075202 (2022).
58. I. Floss, C. Lemell, G. Wachter, V. Smejkal, S. A. Sato, X.-M. Tong, K. Yabana, J. Burgdörfer, Ab initio multiscale simulation of high-order harmonic generation in solids. *Phys. Rev. A* **97**, 011401(R) (2018).
59. M. Vatasescu, Measures of electronic-vibrational entanglement and quantum coherence in a molecular system. *Phys. Rev. A* **92**, 042323 (2015).

Downloaded from https://www.science.org at Institute of Physics, Cas on November 07, 2026

60. M. Vatasescu, Entanglement between electronic and vibrational degrees of freedom in a laser-driven molecular system. *Phys. Rev. A* **88**, 063415 (2013).
61. A. F. Izmaylov, I. Franco, Entanglement in the Born–Oppenheimer approximation. *J. Chem. Theory Comput.* **13**, 20–28 (2017).
62. J. Benjamin, Quantum decoherence and the isotope effect in condensed phase nonadiabatic molecular dynamics simulations. *J. Chem. Phys.* **104**, 5942–5955 (1996).
63. J. Michael, Mean-field dynamics with stochastic decoherence (MF-SD): A new algorithm for nonadiabatic mixed quantum/classical molecular-dynamics simulations with nuclear-induced decoherence. *J. Chem. Phys.* **123**, 234106 (2005).
64. M. Vacher, L. Steinberg, A. J. Jenkins, M. J. Bearpark, M. A. Robb, Electron dynamics following photoionization: Decoherence due to the nuclear-wave-packet width. *Phys. Rev. A* **92**, 040502(R) (2015).
65. G. A. Fiete, E. J. Heller, Semiclassical theory of coherence and decoherence. *Phys. Rev. A* **68**, 022112 (2003).
66. M. Vacher, M. J. Bearpark, M. A. Robb, J. P. Malhado, Electron dynamics upon ionization of polyatomic molecules: Coupling to quantum nuclear motion and decoherence. *Phys. Rev. Lett.* **118**, 083001 (2017).
67. C. Arnold, O. Vendrell, R. Welsch, R. Santra, Control of nuclear dynamics through conical intersections and electronic coherences. *Phys. Rev. Lett.* **120**, 123001 (2018).
68. N. Yoshikawa, T. Tamaya, K. Tanaka, High-harmonic generation in graphene enhanced by elliptically polarized light excitation. *Science* **356**, 736–738 (2017).
69. Y. Kim, M. J. Kim, S. Cha, S. Choi, C.-J. Kim, B. J. Kim, M.-H. Jo, J. Kim, J. Lee, Dephasing dynamics accessed by high harmonic generation: Determination of electron–hole decoherence of dirac fermions. *Nano Lett.* **24**, 1277–1283 (2024).
70. D. Duan, Y. Liu, F. Tian, D. Li, X. Huang, Z. Zhao, Y. Hongyu, B. Liu, W. Tian, T. Cui, Pressure-induced metallization of dense $(H_2S)_2H_2$ with high-Tc superconductivity. *Sci. Rep.* **4**, 6968 (2014).
71. I. Errea, M. Calandra, C. J. Pickard, J. R. Nelson, R. J. Needs, Y. Li, H. Liu, Y. Zhang, Y. Ma, F. Mauri, Quantum hydrogen-bond symmetrization in the superconducting hydrogen sulfide system. *Nature* **532**, 81–84 (2016).
72. R. Taureau, M. Cherubini, T. Morresi, M. Casula, Quantum symmetrization transition in superconducting sulfur hydride from quantum Monte Carlo and path integral molecular dynamics. *NPJ Comput. Mater.* **10**, 56 (2024).
73. I. Errea, M. Calandra, C. J. Pickard, J. Nelson, R. J. Needs, Y. Li, H. Liu, Y. Zhang, Y. Ma, F. Mauri, High-pressure hydrogen sulfide from first principles: A strongly anharmonic phonon-mediated superconductor. *Phys. Rev. Lett.* **114**, 157004 (2015).
74. Z. Wang, Y. Hyunwook Park, H. Lai, X. Junliang, C. I. Blaga, F. Yang, P. Agostini, L. F. DiMauro, The roles of photo-carrier doping and driving wavelength in high harmonic generation from a semiconductor. *Nat. Commun.* **8**, 1686 (2017).
75. C. Heide, Y. Kobayashi, A. C. Johnson, F. Liu, T. F. Heinz, D. A. Reis, S. Ghimire, Probing electron-hole coherence in strongly driven 2D materials using high-harmonic generation. *Optica* **9**, 512–516 (2022).
76. K. Nagai, K. Uchida, S. Kusaba, T. Endo, Y. Miyata, K. Tanaka, Effect of incoherent electron-hole pairs on high harmonic generation in an atomically thin semiconductor. *Phys. Rev. Res.* **5**, 043130 (2023).
77. P. B. Corkum, Plasma perspective on strong field multiphoton ionization. *Phys. Rev. Lett.* **71**, 1994–1997 (1993).
78. J. Zhang, O. Neufeld, N. Tancogne-Dejean, I. T. Lu, H. Hübener, U. de Giovannini, A. Rubio, Enhanced high harmonic efficiency through phonon-assisted photodoping effect. *NPJ Comput. Mater.* **10**, 202 (2024).
79. Y. Liu, R. Long, W.-H. Fang, O. V. Prezhdo, Nuclear quantum effects prolong charge carrier lifetimes in hybrid organic–inorganic perovskites. *J. Am. Chem. Soc.* **145**, 14112–14123 (2023).
80. E. J. Heller, Frozen gaussians: A very simple semiclassical approximation. *J. Chem. Phys.* **75**, 2923–2931 (1981).
81. P. Carlos, Quantum effects in the structural and elastic properties of graphite: Path-integral simulations. *Phys. Rev. B* **104**, 054113 (2021).
82. H. Jiang, X. Tao, M. Kammler, F. Ding, A. M. Wodtke, A. Kandratsenka, T. F. Miller III, O. Bünermann, Small nuclear quantum effects in scattering of H and D from graphene. *J. Phys. Chem. Lett.* **12**, 1991–1996 (2021).
83. A. P. Drozdov, M. I. Eremets, I. A. Troyan, V. Ksenofontov, S. I. Shylin, Conventional superconductivity at 203 kelvin at high pressures in the sulfur hydride system. *Nature* **525**, 73–76 (2015).
84. H. Shi-Qi, D.-Q. Chen, D. Lan-Lin, S. Meng, Solid-state high harmonic spectroscopy for all-optical band structure probing of high-pressure quantum states. *Proc. Natl. Acad. Sci. U.S.A.* **121**, e2316775121 (2024).
85. S. Habershon, D. E. Manolopoulos, T. E. Markland, T. F. Miller III, Ring-polymer molecular dynamics: Quantum effects in chemical dynamics from classical trajectories in an extended phase space. *Annu. Rev. Phys. Chem.* **64**, 387–413 (2013).
86. I. R. Craig, D. E. Manolopoulos, Quantum statistics and classical mechanics, real time correlation functions from ring polymer molecular dynamics. *J. Chem. Phys.* **121**, 3368–3373 (2004).
87. J. Wilhelm, P. Grössing, A. Seith, J. Crewse, M. Nitsch, L. Weigl, C. Schmid, F. Evers, Semiconductor Bloch-equations formalism: Derivation and application to high-harmonic generation from Dirac fermions. *Phys. Rev. B* **103**, 125419 (2021).
88. L. Ortenzi, E. Cappelluti, L. Pietronero, Band structure and electron-phonon coupling in H_3S: A tight-binding model. *Phys. Rev. B* **94**, 064507 (2016).
89. R. Zhao, P. You, S. Meng, Ring polymer molecular dynamics with electronic transitions. *Phys. Rev. Lett.* **130**, 166401 (2023).
90. Y. Li, J. Hao, H. Liu, Y. Li, Y. Ma, The metallization and superconductivity of dense hydrogen sulfide. *J. Chem. Phys.* **140**, 174712 (2014).
91. S. Q. Hu, H. Zhao, C. Lian, X. B. Liu, M. X. Guan, S. Meng, Tracking photocarrier-enhanced electron-phonon coupling in nonequilibrium. *NPJ Quant. Mater.* **7**, 14 (2022).
92. M. Guan, H. Shiqi, H. Zhao, C. Lian, S. Meng, Toward attosecond control of electron dynamics in two-dimensional materials. *Appl. Phys. Lett.* **116**, 043101 (2020).
93. M.-X. Guan, C. Lian, H. Shi-Qi, H. Liu, S.-J. Zhang, J. Zhang, S. Meng, Cooperative evolution of intraband and interband excitations for high-harmonic generation in strained MoS_2. *Phys. Rev. B* **99**, 184306 (2019).
94. G. Kresse, J. Hafner, Ab-initio molecular-dynamics for open-shell transition-metals. *Phys. Rev. B* **48**, 13115–13118 (1993).
95. M. Ceriotti, J. More, D. E. Manolopoulos, i-PI: A Python interface for ab initio path integral molecular dynamics simulations. *Comput. Phys. Commun.* **185**, 1019–1026 (2014).
96. V. Kapil, M. Rossi, O. Marsalek, R. Petraglia, Y. Litman, T. Spura, B. Cheng, A. Cuzzocrea, R. H. Meißner, D. M. Wilkins, B. A. Helfrecht, P. Juda, S. P. Bienvenue, W. Fang, J. Kessler, I. Poltavsky, S. Vandenbrande, J. Wieme, C. Corminboeuf, T. D. Kühne, D. E. Manolopoulos, T. E. Markland, J. O. Richardson, A. Tkatchenko, G. A. Tribello, V. van Speybroeck, M. Ceriotti, i-PI 2.0: A universal force engine for advanced molecular simulations. *Comput. Phys. Commun.* **236**, 214–223 (2019).
97. M. Ceriotti, G. Bussi, M. Parrinello, Nuclear quantum effects in solids using a colored-noise thermostat. *Phys. Rev. Lett.* **103**, 030603 (2009).
98. M. Ceriotti, D. E. Manolopoulos, Efficient first-principles calculation of the quantum kinetic energy and momentum distribution of nuclei. *Phys. Rev. Lett.* **109**, 100604 (2012).

Acknowledgments: We acknowledge D. Chen and P. You for their work and support in code execution framework, parallel optimization, and compatibility. S.H. thanks his spouse, M. Huai, for taking care of the baby, which allowed him to focus on this work. **Funding:** S.M. acknowledges financial support from the Ministry of Science and Technology (grant no. 2021YFA1400200), the National Natural Science Fund of China (grant nos. 12450401 and 12025407), and the Chinese Academy of Sciences (no. YSBR047). S.H. acknowledges financial support from the National Natural Science Fund of China (no. 12304096) and the China Postdoctoral Science Foundation (2022TQ0362). **Author contributions:** Conceptualization: S.H. and S.M. Methodology: S.H., E.W., and R.Z. Investigation: S.H., Q.G., and S.M. Visualization: S.H. Supervision: S.M. Formal analysis: S.H. and Q.X. Resources: Q.G. and S.M. Data curation: S.H., Q.C., and S.M. Validation: S.H., E.W., and S.M. Funding acquisition: S.H. and S.M. Project administration: S.M. Software: Q.C. and S.M. Writing—original draft: S.H. Writing—review and editing: S.H., Q.C., E.W., and S.M. **Competing interests:** The authors declare that they have no competing interests. **Data, code, and materials availability:** All data and code needed to evaluate and reproduce the results in the paper are present in the paper and/or the Supplementary Materials. This study did not generate new materials.

Submitted 23 July 2025
Accepted 2 April 2026
Published 8 May 2026
10.1126/sciadv.aea7877

Downloaded from https://www.science.org at Institute of Physics, Cas on November 07, 2026

ScienceAdvances

Ultrafast decoherence in solid-state high-harmonic generation induced by nuclear-electronic entanglement

Shiqi Hu, Qing Chen, Ruiji Zhao, Qiuhao Xu, Qunfang Gu, En Wang, and Sheng Meng

Sci. Adv. **12** (19), eaea7877. DOI: 10.1126/sciadv.aea7877

View the article online
https://www.science.org/doi/10.1126/sciadv.aea7877
Permissions
https://www.science.org/help/reprints-and-permissions

Downloaded from https://www.science.org at Institute of Physics, Cas on November 07, 2026

Use of this article is subject to the Terms of service

Science Advances (ISSN 2375-2548) is published by the American Association for the Advancement of Science. 1200 New York Avenue NW, Washington, DC 20005. The title *Science Advances* is a registered trademark of AAAS.

Copyright © 2026 The Authors, some rights reserved; exclusive licensee American Association for the Advancement of Science. No claim to original U.S. Government Works. Distributed under a Creative Commons Attribution NonCommercial License 4.0 (CC BY-NC).